

# ACOUSTIC EMISSION SOURCE LOCATION IN A THICK STEEL PLATE BY LAMB MODES

M. A. HAMSTAD

National Institute of Standards and Technology, Materials Reliability Division (853), 325 Broadway, Boulder, CO 80305-3328 and University of Denver, School of Engineering and Computer Science, Department of Mechanical and Materials Engineering, Denver, CO 80208

## Abstract

Through use of a validated finite-element modeling code, buried out-of-plane (two-dimensional code (2D)) and in-plane (three-dimensional code (3D)) acoustic emission (AE) dipole-point-sources were operated at different depths below the top surface of a 25.4-mm (1") thick steel plate with large transverse dimensions. The depths ranged from a source centered at 1.25 mm below the top surface to a source centered at the mid-plane. Most of the cases were run with a source rise time of 2.3  $\mu$ s. For each depth, the out-of-plane displacements were obtained as a function of time at a series of propagation distances up to 1016 mm (40") from the epicenter position for the out-of-plane sources and up to 381 mm (15") for the in-plane sources. The total time for each signal was from the initiation of the source up to 580  $\mu$ s (2D) and 200  $\mu$ s (3D). Since the displacements were obtained on both the top and bottom surfaces, results representing sources at various depths over the whole plate thickness were available. The modeled signals were examined with no filtering as well as with a 40-kHz high-pass filter or a bandpass filter of 100 kHz to 300 kHz. In order to correlate the AE displacement signals with Lamb modes, the relevant group-velocity curves were superimposed on wavelet transforms of the signals. Modal regions that carried a significant portion of the AE energy were identified by mode, frequency range and source depth. For sources located near the plate top surface, a Rayleigh wave was observed in the top-surface displacement signals. This wave was not present in the signals obtained from the bottom surface or from sources not located near the top surface. Signal arrival times at different propagation distances were obtained from the maximum wavelet transform (WT) coefficients at key frequencies of certain modes. Plots of propagation distance versus arrival times were used to find group velocities for a key frequency/mode combination (102 kHz for either the  $A_0$  or  $S_0$  Lamb modes). These velocities were found to be very close to those obtained from Lamb-wave theory. A method to identify the mode that led to the WT peak at the key frequency was demonstrated for AE events that were detected at four sensors in an array. This method could be automated to process digitized signals to significantly improve accuracy of source location in thick plates when nonresonant AE sensors are used.

**Keywords:** Acoustic emission arrival times, AE dipoles, finite element modeling, Lamb waves, source location, wavelet transform.

## Introduction

The author and his co-workers have published a number of papers on the analysis of finite-element-modeled (FEM) acoustic emission (AE) signals in a 4.7-mm thick aluminum plate [1 - 4]. In this thin plate, only the two fundamental modes ( $A_0$  and  $S_0$ ) were significantly excited over the range of typical frequencies used in AE. One focus of this prior work was the use of a wavelet transform (WT) to obtain accurate arrival times of certain frequencies of the two fundamental modes. Since these arrival times were all associated with specific known group velocities,

accurate source locations could be calculated from the dispersive AE signals even in the presence of significant electronic preamplifier noise [3].

Over the last several years we have been creating an FEM database of AE signals for a 25.4-mm thick steel plate. The purpose of the research reported here was to apply a WT to identify certain important Lamb-wave modal regions and to extract accurate signal arrival times from these regions for the purpose of the calculation of source locations. A recent publication [5] considered the question of the extraction of arrival times in nominal 15-mm thick steel determined by use of the maximum magnitude of WT coefficients at certain frequencies. “Mathematically calculated” [5] waveforms that had been filtered to simulate a 150-kHz resonant sensor were studied. Experimental results also were obtained from a cylindrical steel pressure vessel with an outer diameter of 800 mm and a wall thickness of 15.5 mm. Experimental waveforms from both pressurization-activated sources and pencil-lead breaks were obtained with resonant (frequency of 150 kHz) AE sensors. The results indicated some success and some difficulties for maximum propagation distances of up to 360 mm.

### Finite-Element Modeled AE Signal Database

To create the finite-element database used in this research, an axially symmetric (2D) code was primarily used. This choice allowed propagation distances up to 1016 mm (40 in) without extremely long parallel-processor computer runs. The domain size was large enough that reflections from the edges of the flat plate did not occur during the duration of the direct-path signal. For particular comparisons, some results with a 3D code (with an appropriate large domain size) were also used. The validations of the explicit finite-element codes can be found in published literature [6, 7].

The entire FEM signals were either left unfiltered or numerically processed with a 40-kHz (four-pole Butterworth) high-pass filter or a similar bandpass filter of 100 kHz to 300 kHz. Subsequently, all the signals were resampled from the original time step (see Table 1) to 0.1  $\mu$ s per point. This rate corresponds to typical sampling rates used to capture waveforms in AE experiments. The AE signals were examined out to 580  $\mu$ s after the source initiation time for the 2D code and 200  $\mu$ s for the 3D code. The sources in the continuous mesh domain were dipoles (self-equilibrating forces from two single-cell body-force monopoles each acting on one cell, with one cell between them) using the “equivalent body force” concept for displacement discontinuities [8]. The forces were applied with a “cosine bell” temporal dependence  $T(t)$  given by

$$T(t) = \begin{cases} 0 & \text{for } t < 0, \\ (0.5 - 0.5 \cos [\pi t / \tau]) & \text{for } 0 \leq t \leq \tau, \text{ and} \\ 1 & \text{for } t > \tau, \end{cases} \quad (1)$$

where  $\tau = 2.3 \mu$ s was the source rise time for most of the cases. One run was made with a 1.5- $\mu$ s rise time to check for significant changes in the higher signal frequencies with a shorter source rise time. No significant changes were observed. The finite-element calculations were made based on bulk velocities and density values for steel (longitudinal velocity = 5940 m/s, shear velocity = 3220 m/s and density = 7.8 kg/m<sup>3</sup>) [9]. Based on our previous experience, the uniform cell size was smaller for sources that were nearer to the plate surface for the 2D runs that were primarily used in this research. This change was made due to the presence of Rayleigh waves in those cases. Table 1 shows the source orientations, propagation distances, source depths (depth of center of source below the top surface of the plate), uniform cell sizes, and time steps of the finite-element calculations. The AE signals from single nodes provided the out-of-plane top-surface and bottom-surface displacement versus time corresponding to a perfect point-contact

sensor (pseudo-sensor) at a series of propagation distances. The use of bottom surface nodes extended the source depths shown in Table 1 without materially changing the code run times. For example, the source at a depth of 1.25 mm below the top surface corresponds to a source at a depth of 24.15 mm above the bottom surface when the bottom surface displacement signal was used. In essence, one computer run provided two depths. In the case of the 3D runs, the pseudo-sensors were located in the zero-degree propagation direction (the in-plane x-axis direction at several propagation distances up to 381 mm (15'') from the source epicenter. The in-plane dipole forces were also aligned in this direction.

Table 1 Description of finite-element database used in this study.

Source type	Depth of source below top surface (mm)	FEM: Cell size (mm) / time step (ns)
Out-of-plane dipole with propagation distances (in mm) of 127, 254, 381, 508, 635, 762, 1016 (2D code)	1.25	0.125 / 18.9
	4.73	0.249 / 37.7
	7.72	0.498 / 75.5
	10.71	0.498 / 75.5
	12.7	0.498 / 75.5
In-plane and out-of-plane dipoles with propagation distance of 381 mm (3D code)	1.25	0.498 / 75.5
	7.72	0.498 / 75.5
	12.7	0.498 / 75.5

### Wavelet Transform Information

Wavelet transform results were used to enhance the identification of the AE signal Lamb modes and to obtain from WT coefficient peaks the different mode arrival times at key frequencies. The WT results were obtained using the AGU-Vallen Wavelet freeware [10] with the key parameter settings being: maximum frequency = 500 kHz, frequency resolution = 2 kHz and wavelet size = 600 samples. The Wavelet Time range settings for the number of samples (i.e., points) were up to about 5800 points, allowing the full-direct-arrival signal to be transformed for the out-of-plane source runs. For the in-plane sources a total of about 2500 points was used so as to fully correspond to the group velocity curves at the maximum propagation distance. In the color WT figures, the red color (surrounded by yellow) indicates the highest intensity region of the WT coefficients. In a black-and-white print out of the color results, the darkest region inside a lighter region indicates the high intensity region.

### Group Velocity Curves for Thick Steel Plate

Using the bulk velocities and density provided above, the group velocity curves were calculated [11, 12]. The results are shown in Fig. 1 for the first five symmetric and anti-symmetric modes. Due to the many potential modes that are present in the typical frequency range of AE interest, this figure shows that there may be potential difficulties in mode identification in frequency regions where the group velocities are similar. This situation will be particularly true when the propagation distances are not large, since for many frequencies the arrival times of the various modes will not be widely separated in time. Thus, it was initially desirable to study signals for propagation distances that were fairly large in order to more easily distinguish different modes. Due to limitations on availability of computing resources for long runs, it was decided to use signals obtained from the 2D code for propagation distances up to 1016 mm (40''). The 2D code can be used to calculate cases only for axisymmetric out-of-plane sources in plates, whereas many real AE sources in metals can be primarily represented by in-plane dipoles. To establish

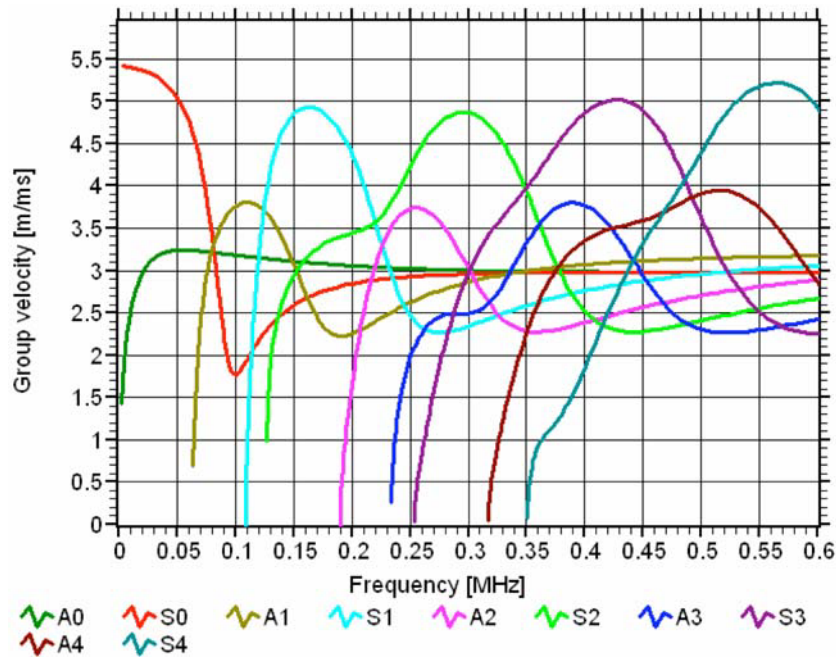


Fig. 1 Group velocities versus frequency for a steel plate of 25.4-mm thickness; first five symmetric and anti-symmetric modes shown.

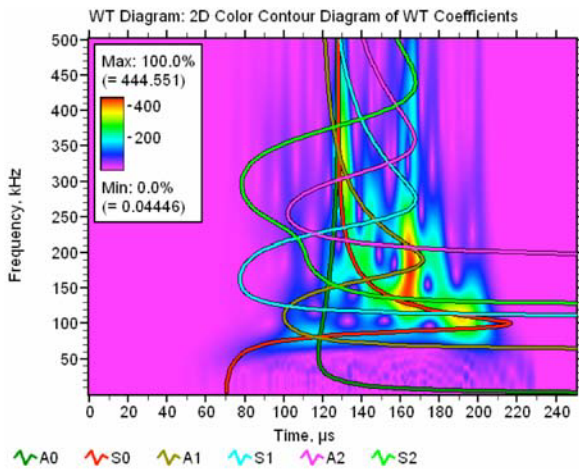


Fig. 2 WT for out-of-plane dipole at a depth of 7.72 mm below the surface, 40-kHz high-pass, 3D code.

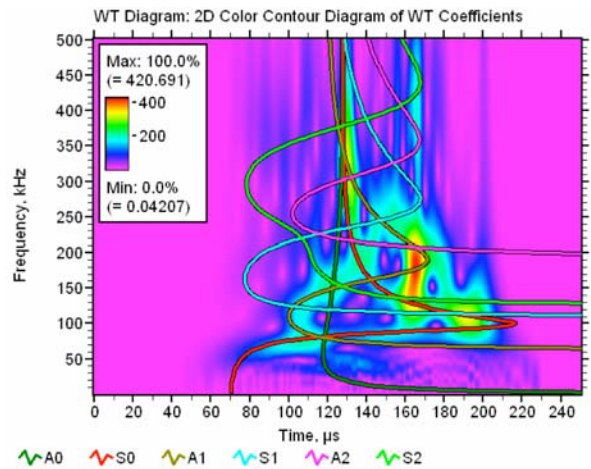


Fig. 3 WT for in-plane dipole at a depth of 7.72 mm below the surface, 40-kHz high-pass, 3D code.

whether the analysis results with the 2D code signals could be extended to in-plane source signals, we considered some comparisons of the displacement signals from out-of-plane dipole sources with in-plane dipole sources at a propagation distance of 381 mm in the next section.

### Modes Excited by Out-of-Plane versus In-Plane Buried Dipoles

Figures 2 and 3 respectively show WTs of the displacement signals (top surface) from out-of-plane and in-plane (both 3D code) buried dipoles at a depth of 7.72 mm below the top surface of the plate. The out-of-plane displacements were obtained at a propagation distance of 381 mm. The WT results were obtained from the signals after applying a 40-kHz high-pass filter. The WT results have been superimposed with the first three symmetric and anti-symmetric Lamb modes.

Examination of these two figures shows that the modal intensity distribution is quite similar, particularly for the three regions with the highest WT intensity. Thus, we can expect that certain results determined from the analysis of the signals with out-of-plane dipole sources can be transferred to the signals from in-plane dipole sources.

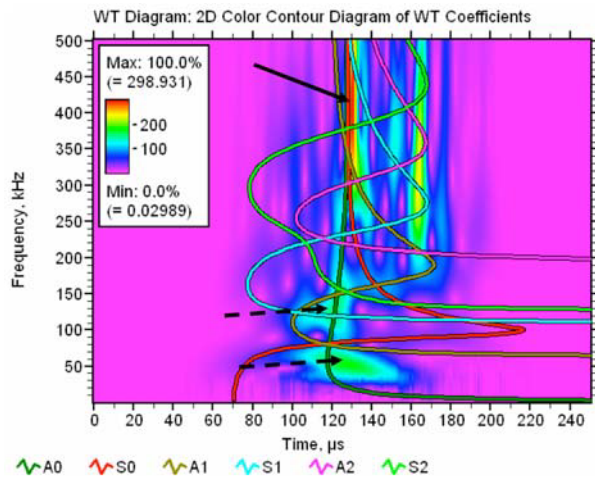


Fig. 4 WT for out-of-plane dipole at a depth of 1.25 mm below the surface, 40-kHz high-pass, 3D code.

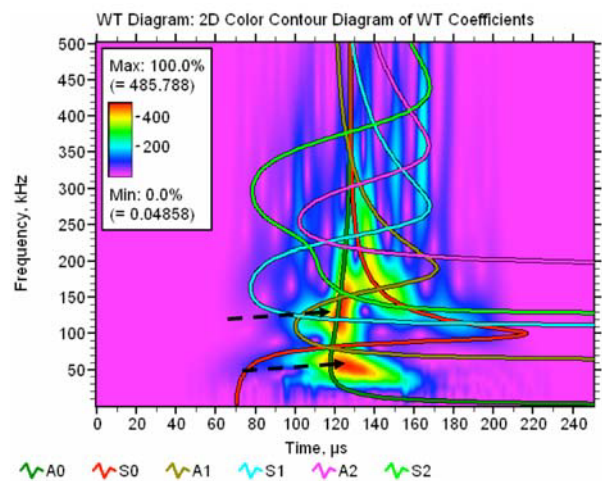


Fig. 5 WT for in-plane dipole at a depth of 1.25 mm below the surface, 40-kHz high-pass, 3D code.

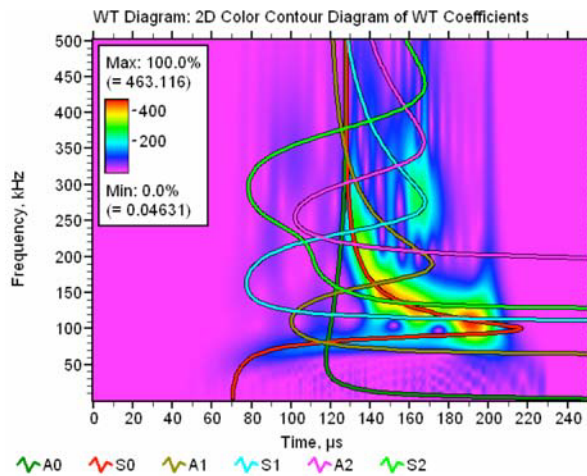


Fig. 6 WT for out-of-plane dipole at a depth of 12.7 mm below the surface, 40-kHz high-pass, 3D code.

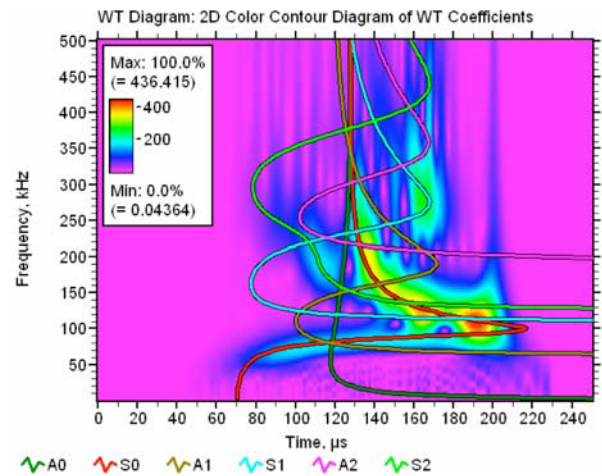


Fig. 7 WT for in-plane dipole at a depth of 12.7 mm below the surface, 40-kHz high-pass, 3D code.

The comparison of the out-of-plane and in-plane source-generated signals at the same propagation distance for depths nearer the surface (1.25 mm) and at the mid-plane (12.7 mm) demonstrate some similarities and some differences. Figures 4 and 5 (both 3D code) show the signals from the two orientations at a depth of 1.25 mm, and Figs. 6 and 7 (both 3D code) illustrate the displacement signals at a depth of 12.7 mm. At the 12.7-mm depth, the WT results are nearly identical for the two source orientations. The main differences between the two source orientations appear for a source at a depth of 1.25 mm. Figure 4 (out-of-plane) shows a high-frequency Rayleigh wave (see solid arrow) with the highest intensity at frequencies above about 340 kHz. Also in Fig. 4, there is a region of lesser intensity associated with the  $A_2$  and  $S_1$  modes at frequencies above about 250 kHz. These two regions do not appear with high intensity for the in-

plane source orientation. But the lower frequency regions of highest intensity for the in-plane case (see dashed arrows in Fig. 5) do have similar regions for the out-of-plane case (see dashed arrows in Fig. 4). In Fig. 5, these lower frequency regions do not stand out, due to the higher intensity of the high frequency regions. Thus, if only the lower-frequency regions are considered, we can expect that most of the analysis results for out-of-plane source-based signals can be extended to in-plane source-based signals. In the later sections of this paper, the emphasis will be on lower frequency regions; thus the differences noted here will not be important factors in extending the results from out-of-plane sources to in-plane ones.

### **Displacement Signals and WT Results at 1016 mm Propagation Distance for Out-of-Plane Dipoles**

Figures 8, 9 and 10 respectively show at a propagation distance of 1016 mm the out-of-plane displacement versus time (as a function of the out-of-plane source depth below the surface of the pseudo-sensor) for the conditions of no filtering, 40-kHz high-pass and 100-kHz to 300-kHz bandpass (note that the fastest part of the  $S_0$  mode requires about 180  $\mu$ s to reach the 1016-mm propagation distance). The corresponding WT results are shown in Figs. 11, 12 and 13 (for convenience in making comparisons arranged in the figures so that depths at symmetric distances from the midplane are next to each other). Some general observations based on these figures follow. First, as can be seen in Figs. 8 and 11 for sources nearer either surface (depths (in mm) of 1.25, 4.73, 20.67 and 24.15), considerable energy was present in the lowest frequency portion of the  $A_0$  mode (see circled regions in Fig. 11) when no filter was applied. This result is similar to what we found in the 4.7 mm aluminum plate studies [13]. But there is an important difference. The frequencies with significant energy in this portion of the  $A_0$  mode are less than 40 kHz in the 25.4-mm thick plate. These frequencies are below the frequencies normally used in AE monitoring. Thus, only in the case of a test environment that is free of significant low-frequency extraneous noise (coupled with the use of AE sensors with good sensitivity in the 10-kHz to 40-kHz frequency range) could this portion of the  $A_0$  mode be exploited for AE monitoring.

Second, the signal displacements in Figs. 8, 9 and 10 show that the signal amplitudes increase gradually (from about 180  $\mu$ s) with increasing time, and they reach their highest amplitudes later in the signals. Thus, AE approaches that depend on threshold penetration for the determination of arrival times are likely to provide a set of arrival times that correspond to a wide variety of propagation velocities as a function of different propagation distances and/or source intensities. This result will be particularly true for larger propagation distances.

Third, even at the fairly large propagation distance of 1016 mm, there likely will still be difficulties in the determination of the mode that corresponds to a WT magnitude peak at frequencies above about 120 kHz due to multiple regions with intensities that change with different source depths as shown in WTs of Figs. 11, 12 and 13. Thus, for a source location calculation, it may not be clear as to which group velocity should be used for a certain set of WT-determined arrival times at frequencies above 120 kHz.

Fourth, as indicated by the solid arrows in Figs. 8 and 9 (see also Figs. 11 and 12), the Rayleigh wave (with frequencies above about 340 kHz) clearly appears in the displacement signals from sensors on a surface, only when the source is close to that surface (1.25 mm below the top surface, in this case). In the WT results for a source depth of 4.73 mm, the Rayleigh wave can still be observed (see solid arrows in Figs. 11 and 12), but it is not as easily observed in the displacement signals from the source at this depth.

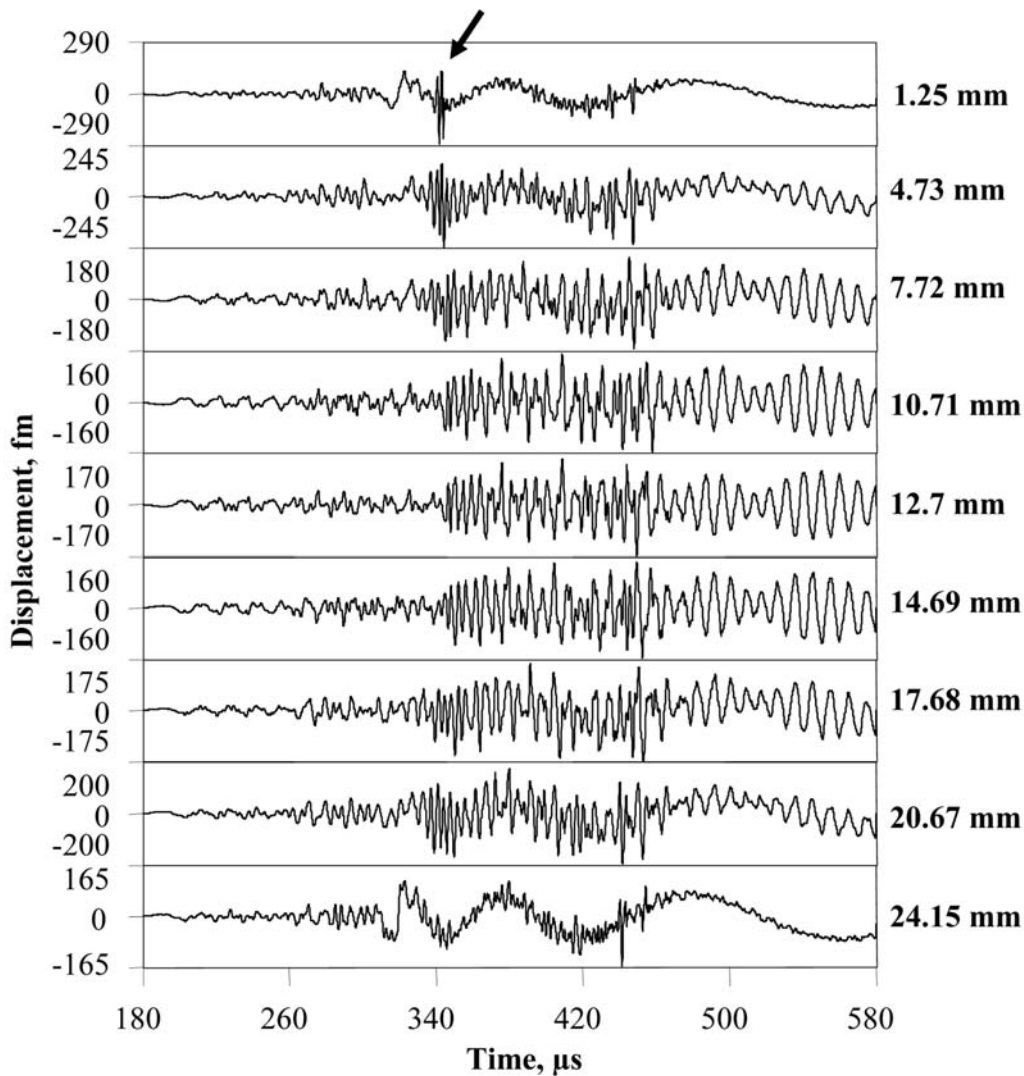


Fig. 8 Out-of-plane displacement vs. time at 1016 mm, out-of-plane source at depths shown below the top surface (location of pseudo-sensor), no filter.

Fifth, sources near the midplane of the plate had a WT maximum at about 100 kHz for the  $S_0$  mode, as can be seen in the WT Figs. 11, 12 and 13 at the source depths of 4.73 mm through 20.63 mm (see dashed arrows). The relative intensity of this region becomes more dominant at source depths nearer the plate midplane. Since a WT maximum in this frequency range occurs for many depths and all three filter ranges, this frequency may be useful for the determination of arrival times. Sixth, for some source depths nearer the midplane, the AE displacement signals and their WTs become more similar for depths symmetric about the midplane of the plate.

The WT results shown in Figs. 11, 12 and 13 were examined to identify potential higher intensity mode and frequency regions that might be used to determine arrival times that could be associated with particular group velocities. Table 2 summarizes this information with the highest intensities listed first for each source depth. The table does not include high intensity regions where the mode could not be clearly distinguished. This situation occurred most often at higher frequencies for some source depths. Since a key goal of this research was to determine key frequencies associated with specific modes that could be used to determine accurate arrival times corresponding to a known group velocity, the next section attempts to identify useful frequency/mode combinations for this purpose.

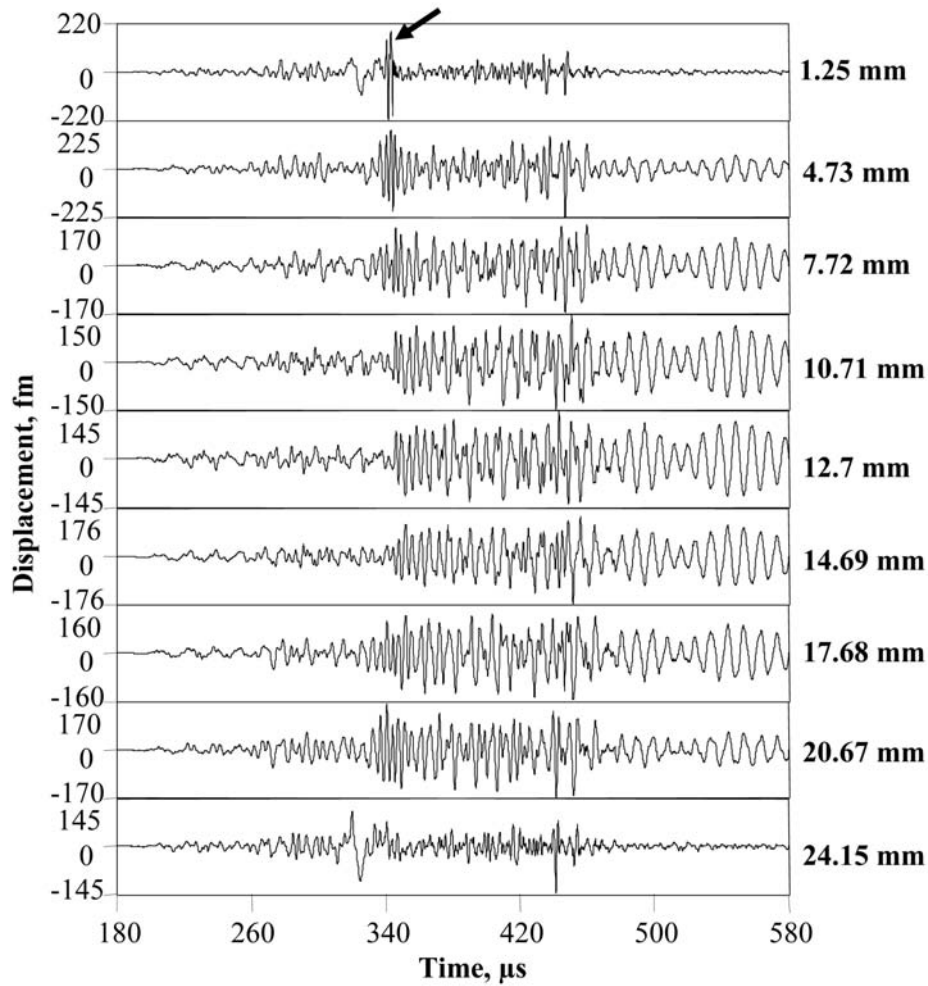


Fig. 9 Out-of-plane displacement vs. time at 1016 mm, out-of-plane source at depths shown below the top surface (location of pseudo-sensor), 40-kHz high-pass filter.

Table 2 Modes and frequency with larger WT magnitudes after 1016 mm of propagation.

Source depth (mm)	Anti-symmetric modes: mode/frequency (kHz)			Symmetric modes: mode/frequency (kHz)		
	No filter	40 kHz high-pass	100 to 300 kHz	No filter	40 kHz high-pass	100 to 300 kHz
1.25	A <sub>0</sub> /20; A <sub>0</sub> /420	A <sub>0</sub> /420; A <sub>0</sub> /52	A <sub>0</sub> /318; A <sub>0</sub> /352	—	—	—
4.73	A <sub>0</sub> /374; A <sub>0</sub> /14	A <sub>0</sub> /374	A <sub>1</sub> /192	S <sub>0</sub> /102	S <sub>0</sub> /102	S <sub>0</sub> /102
7.72	A <sub>1</sub> /186	A <sub>1</sub> /186	A <sub>1</sub> /186	S <sub>0</sub> /102	S <sub>0</sub> /102	S <sub>0</sub> /102
10.71	—	—	—	S <sub>0</sub> /102	S <sub>0</sub> /102	S <sub>0</sub> /102
12.7 mid-plane	—	—	—	S <sub>0</sub> /102; S <sub>1</sub> /276	S <sub>0</sub> /102; S <sub>1</sub> /276	S <sub>0</sub> /102; S <sub>1</sub> /272
14.69	—	—	—	S <sub>0</sub> /102	S <sub>0</sub> /102	S <sub>0</sub> /102
17.68	A <sub>1</sub> /182	A <sub>1</sub> /182	A <sub>1</sub> /184	S <sub>0</sub> /102	S <sub>0</sub> /102	S <sub>0</sub> /102
20.67	A <sub>0</sub> /278	A <sub>0</sub> /186; A <sub>1</sub> /278	A <sub>0</sub> /266; A <sub>1</sub> /186	S <sub>0</sub> /102	S <sub>0</sub> /102; S <sub>0</sub> /268	S <sub>0</sub> /102; S <sub>0</sub> /256
24.15	A <sub>0</sub> /20	A <sub>0</sub> /54	A <sub>0</sub> /138	—	—	—

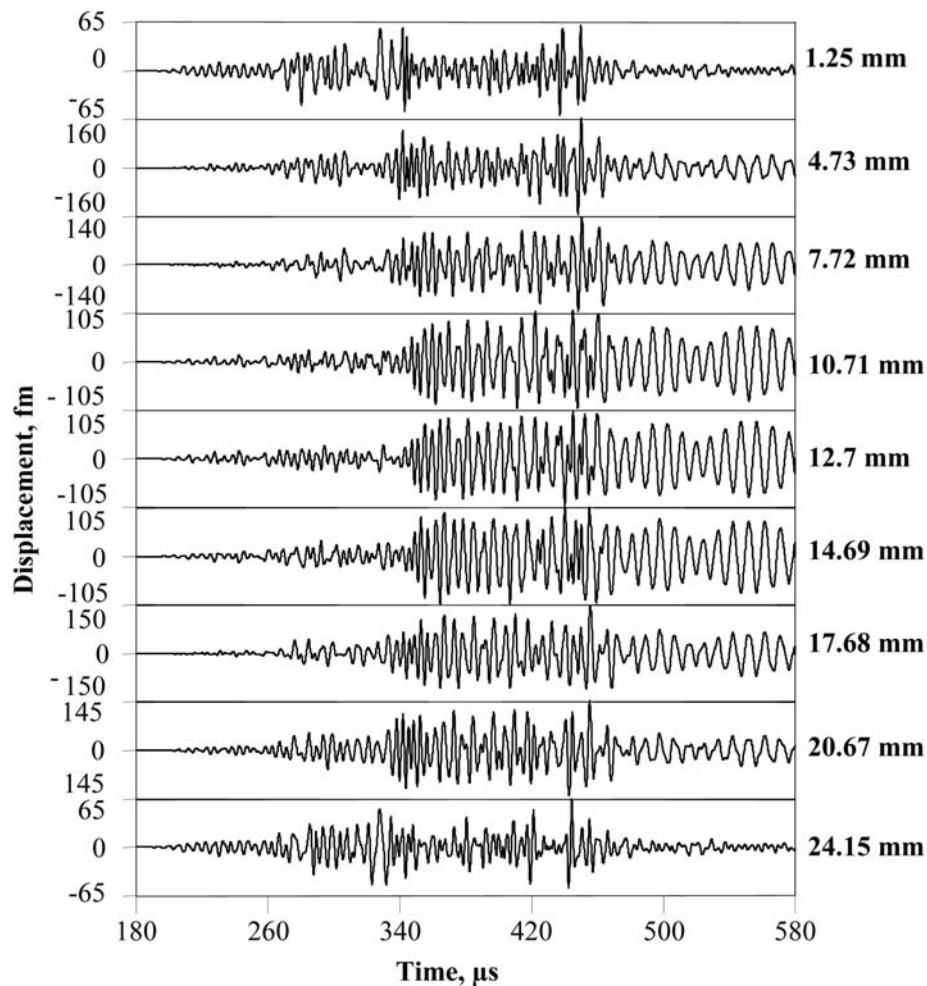


Fig. 10 Out-of-plane displacement vs. time at 1016 mm, out-of-plane source at depths shown below the top surface (location of pseudo-sensor), 100 to 300 kHz filter.

### Useful Frequency/Mode Combinations to Determine Arrival /Times

Examination of the information in Table 2 demonstrates that the highest intensity (largest WT coefficients) mode/frequency combinations change as a function of source depth. There are four conditions that might be used to guide the selection of frequency/mode combinations that could be most useful to determine arrival times. First is the selection of frequencies that would be applicable for all three frequency ranges considered here. Second, frequency/mode combinations that cover a wide range of source depths for each combination are desirable. Third, the mode corresponding to each of the selected frequencies should be separated from any alternate mode(s) with intensity at these frequencies by a considerable amount of propagation time (or equivalently have group velocities that are significantly different). Finally, as is obvious, the WT maximum(s) at the frequencies selected should correspond to the mode arrivals.

To best meet the conditions listed above, the frequency selected was 102 kHz. This frequency can be associated only with the  $A_0$ ,  $A_1$  or the  $S_0$  modes, and it is possible to use this choice for all three of the frequency ranges. Further, as will be seen below, the  $A_1$  mode did not provide a peak of the WT coefficients at this frequency, and the group velocities associated with the  $A_0$  and  $S_0$  mode peaks are very different at 102 kHz. It should be noted that the combination of  $A_0/102$  kHz is not among the most intense modal regions at the 1.25 mm and 24.15 mm

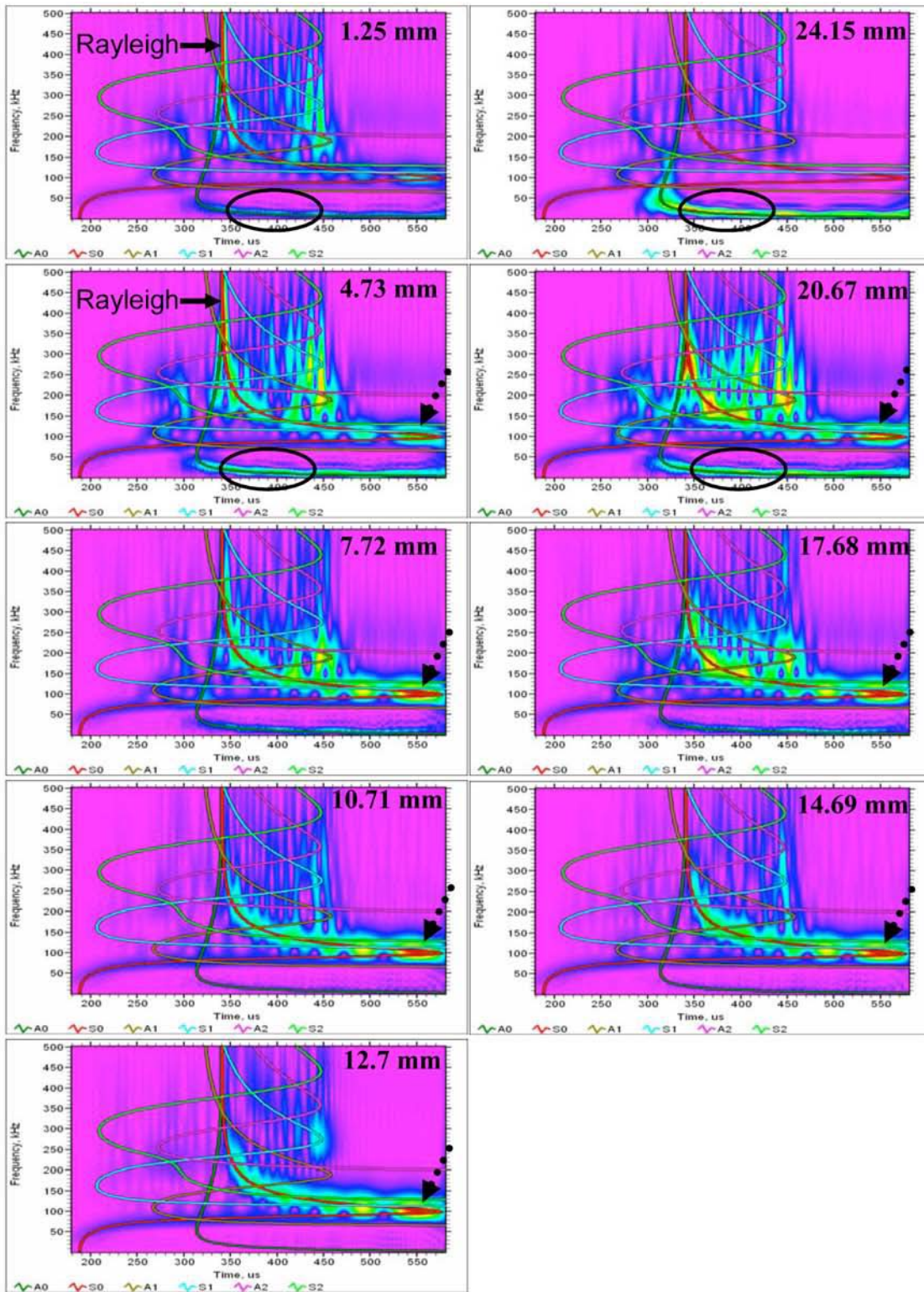


Fig. 11 WTs of Fig. 8 with superimposed group velocities, at indicated depths, 180  $\mu$ s to 570  $\mu$ s horizontal scale, 0 kHz to 500 kHz vertical scale.

depths. But, since earlier work [3] demonstrated that accurate arrival times could be determined at low signal-to-noise ratios, the lower intensity of this combination at these depths is not expected to be detrimental to its use.

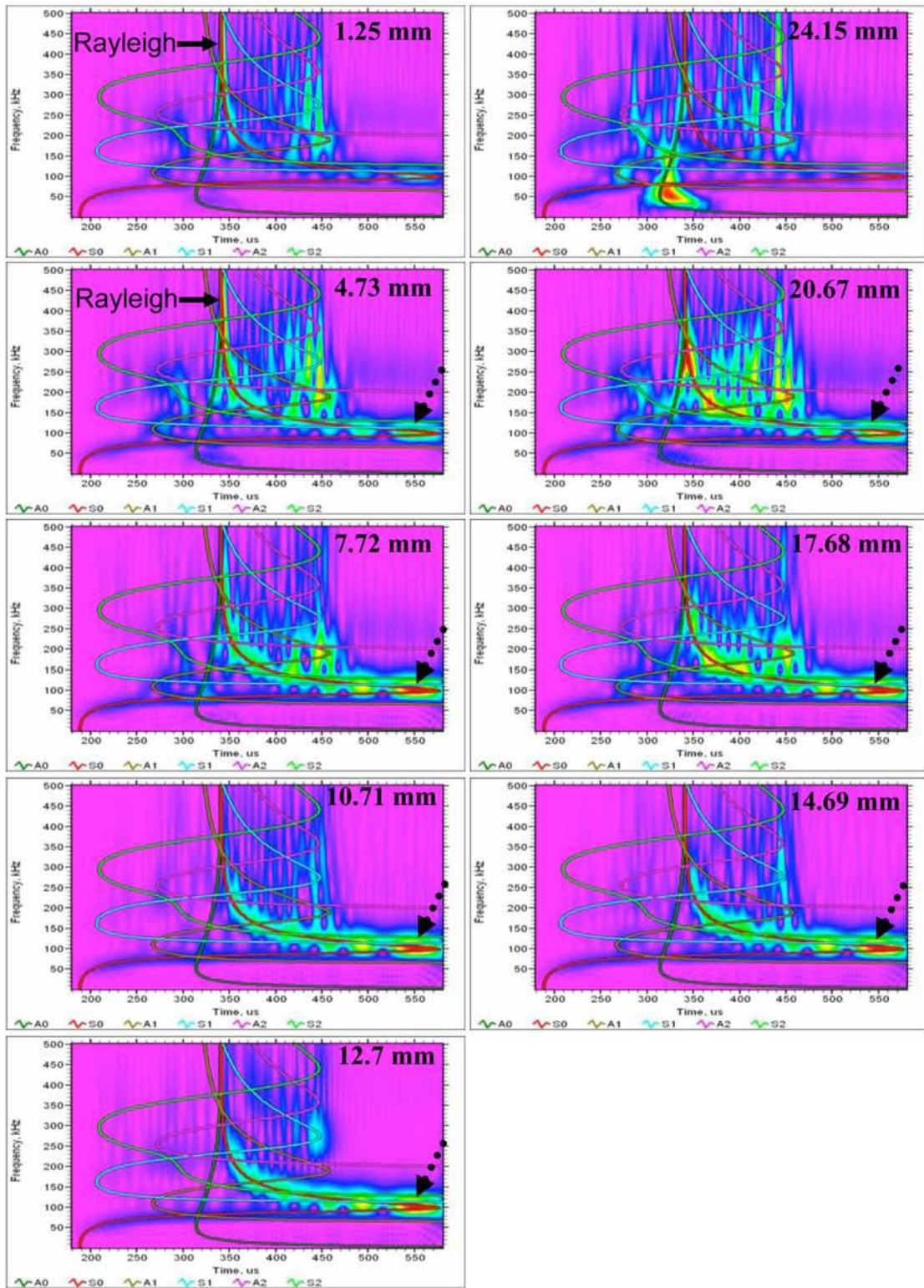


Fig. 12 WTs of Fig. 9 with superimposed group velocities, at indicated depths, 40-kHz high-pass, 180  $\mu$ s to 570  $\mu$ s horizontal scale, 0 kHz to 500 kHz vertical scale.

For all the source depths and propagation distances the arrival times, Table 3 provides the mode and the WT peak magnitude percentage (relative to the signal overall peak WT magnitude) at a frequency of 102 kHz for the 40 kHz high-pass data. Figure 14 shows (from top to bottom) a

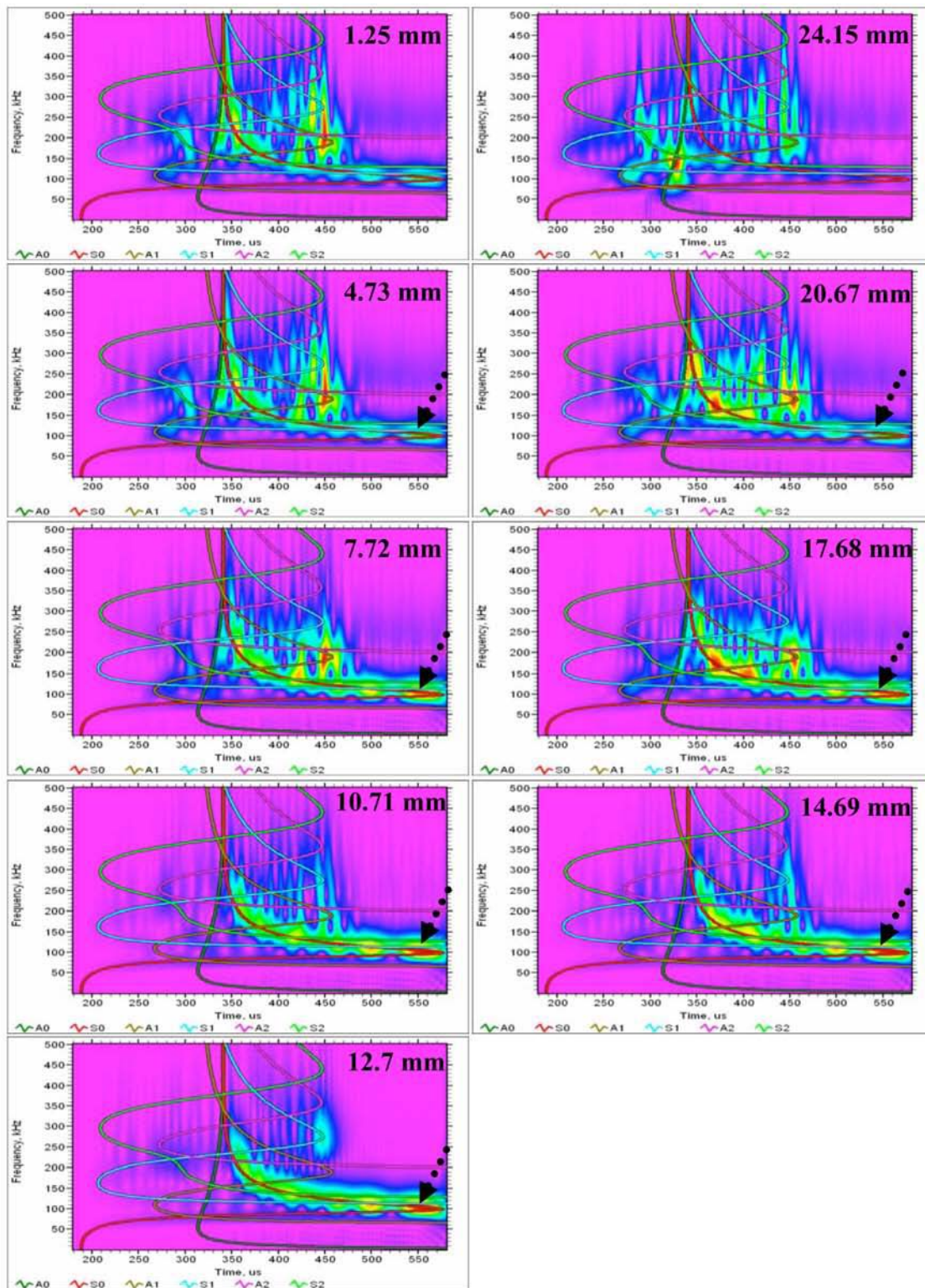


Fig. 13 WTs of Fig. 10 with superimposed group velocities, at indicated depths, 100 kHz to 300 kHz, 180  $\mu$ s to 570  $\mu$ s horizontal scale, 0 kHz to 500 kHz vertical scale.

typical AE displacement signal, a plot of the WT coefficients at 102 kHz versus time that lead to the maximum and associated arrival time (in this case from the  $S_0$  mode), and the corresponding WT. The data in this figure are from a source depth of 7.72 mm and a propagation distance of

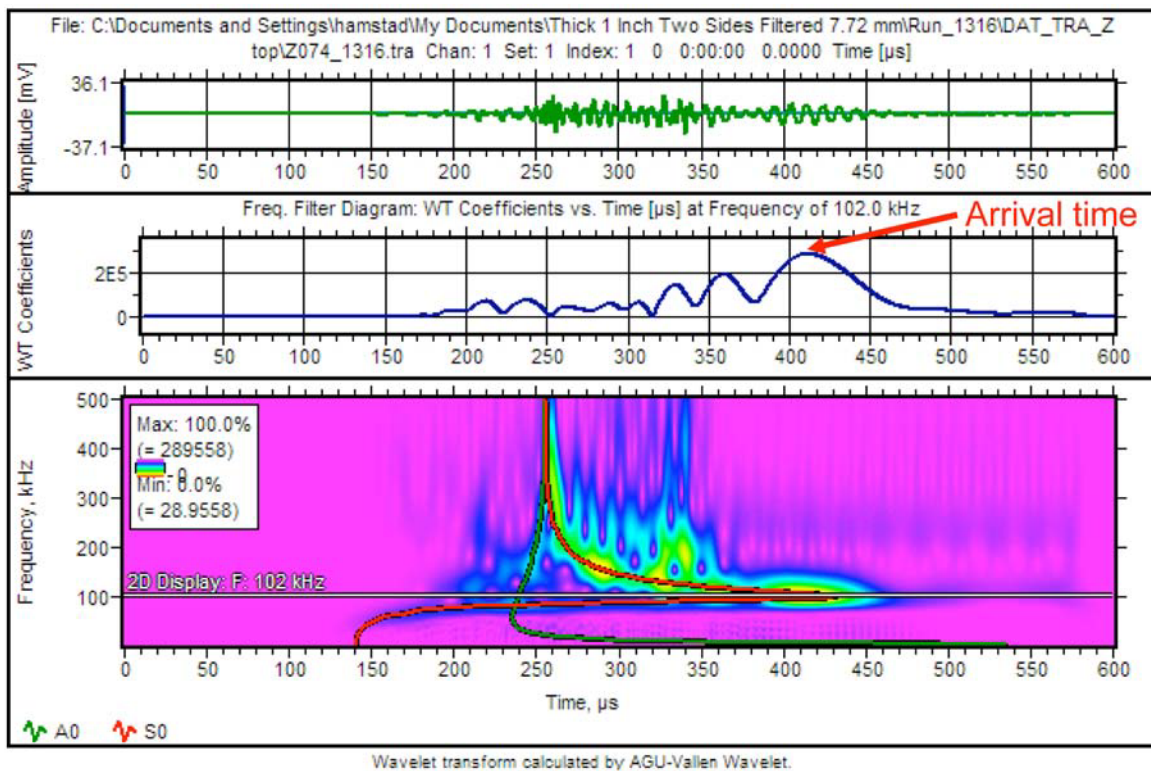


Fig. 14 Example from top to bottom of the signal, plot of the WT coefficients that lead to the peak arrival time (see arrow) at 102 kHz and the wavelet transform with group velocity curves at a propagation distance of 762 mm and a source depth of 7.72 mm.

762 mm. In addition, Table 3 lists the group velocities as directly determined from the slope of a plot of propagation distance versus the arrival times in the table. Finally, these group velocities can be compared in the table to the velocities (last column) determined from the group velocity curves (theory) for the relevant modes. The results in Table 3 show that group velocities very close to the theoretical values can be determined for the only two modes,  $A_0$  and  $S_0$  that produced the peak in the WT magnitude at 102 kHz. Results similar to those in Table 3 were obtained for the other two frequency ranges. The group velocity results for these two frequency ranges are summarized in Table 4 along with the “theory” velocities from the group velocity curves. The results show that the plots of propagation distance versus the arrival times again provide group velocities close to the theoretical values for these two frequency ranges. The maximum difference from the group velocity as determined by the group velocity curves and that from the slope of plots of distance versus arrival time was less than 3% for all three frequency ranges. These results imply that arrival times determined by the peak of the WT at 102 kHz accurately correspond to the relevant mode arrivals.

Of special interest was the fact that the data points for 127-mm propagation distance arrival time fit directly on the linear line that defined the group velocity obtained from the FEM data. Figures 15 (a) and (b) show typical plots (no filter data) for the propagation distance versus the arrival time for both the relevant mode cases, and they include the straight-line least-squares fit. It is worth noting that, at the 127-mm propagation distance, the ratio of distance over the plate thickness is only 5. It often has been assumed that a ratio of at least 10 could be required to fully develop Lamb waves [14].

Table 3 At 102 kHz, WT peak arrival times ( $\mu\text{s}$ ), mode and percentage of peak WT magnitude for 40 kHz high-pass data.

Source depth (mm)	Propagation distance (mm)							Group velocity (mm/ $\mu\text{s}$ ) from slope	Group velocity (mm/ $\mu\text{s}$ ) from theory
	127	254	381	508	635	762	1016		
1.25	41.9, A <sub>0</sub> , 81	78.5, A <sub>0</sub> , 98	123., A <sub>0</sub> , 42	162.5, A <sub>0</sub> , 55	200.8, A <sub>0</sub> , 52	243.2, A <sub>0</sub> , 55	321.3, A <sub>0</sub> , 48	3.16	3.18
4.73	64.7, S <sub>0</sub> , 54	131.2, S <sub>0</sub> , 74	198.9, S <sub>0</sub> , 55	269.2, S <sub>0</sub> , 88	339.6, S <sub>0</sub> , 68	410.2, S <sub>0</sub> , 61	549.3, S <sub>0</sub> , 65	1.83	1.78
7.72	64.7, S <sub>0</sub> , 95	131.0, S <sub>0</sub> , 97	198.8, S <sub>0</sub> , 100	269.9, S <sub>0</sub> , 96	341.4, S <sub>0</sub> , 100	411.2, S <sub>0</sub> , 100	549.5, S <sub>0</sub> , 100	1.83	1.78
10.71	64.7, S <sub>0</sub> , 95	130.9, S <sub>0</sub> , 99	198.8, S <sub>0</sub> , 100	270.2, S <sub>0</sub> , 100	342.2, S <sub>0</sub> , 100	411.7, S <sub>0</sub> , 100	548.8, S <sub>0</sub> , 100	1.83	1.78
12.7	64.7, S <sub>0</sub> , 95	130.9, S <sub>0</sub> , 99	198.8, S <sub>0</sub> , 100	270.2, S <sub>0</sub> , 100	342.4, S <sub>0</sub> , 100	411.8, S <sub>0</sub> , 100	548.7, S <sub>0</sub> , 100	1.83	1.78
14.69	64.7, S <sub>0</sub> , 95	130.9, S <sub>0</sub> , 99	198.9, S <sub>0</sub> , 100	270.1, S <sub>0</sub> , 100	342.3, S <sub>0</sub> , 100	411.7, S <sub>0</sub> , 100	548.8, S <sub>0</sub> , 100	1.83	1.78
17.68	64.8, S <sub>0</sub> , 81	130.9, S <sub>0</sub> , 100	199.0, S <sub>0</sub> , 87	269.6, S <sub>0</sub> , 100	341.6, S <sub>0</sub> , 100	411.1, S <sub>0</sub> , 100	548.9, S <sub>0</sub> , 100	1.83	1.78
20.67	65.0, S <sub>0</sub> , 57	131.2, S <sub>0</sub> , 63	199.1, S <sub>0</sub> , 62	268.8, S <sub>0</sub> , 60	340.1, S <sub>0</sub> , 60	409.9, S <sub>0</sub> , 67	549.5, S <sub>0</sub> , 76	1.83	1.78
24.15	37.5, A <sub>0</sub> , 50	81.6, A <sub>0</sub> , 67	122.3, A <sub>0</sub> , 76	163.6, A <sub>0</sub> , 59	203.2, A <sub>0</sub> , 80	242.8, A <sub>0</sub> , 74	323.1, A <sub>0</sub> , 76	3.13	3.18

Table 4 Summary of slope-determined group velocity results for no-filter and 100 kHz to 300 kHz data.

Source depth (mm) and mode of WT peak at 102 kHz	Group velocity (mm/ $\mu\text{s}$ ) from slope for no-filter data	Group velocity (mm/ $\mu\text{s}$ ) from slope for 100 kHz to 300 kHz filter data	Group velocity (mm/ $\mu\text{s}$ ) from group velocity curves ("theory")
1.25, A <sub>0</sub>	3.16	3.15	3.18
4.73, S <sub>0</sub>	1.83	1.83	1.78
7.72, S <sub>0</sub>	1.83	1.83	1.78
10.71, S <sub>0</sub>	1.83	1.83	1.78
12.7, S <sub>0</sub>	1.83	1.83	1.78
14.69, S <sub>0</sub>	1.83	1.83	1.78
17.68, S <sub>0</sub>	1.83	1.83	1.78
20.67, S <sub>0</sub>	1.83	1.83	1.78
24.15, A <sub>0</sub>	3.13	3.10	3.18

Further, Fig. 16 shows the wide variation in the signal durations for the different propagation distances. The primary part of the signals varied in duration from about 50  $\mu\text{s}$  to about 400  $\mu\text{s}$  as the propagation distance increased from 127 mm to 1016 mm. Further, over this range of distances The primary part of the signals varied in duration from about 50  $\mu\text{s}$  to about 400  $\mu\text{s}$  as the

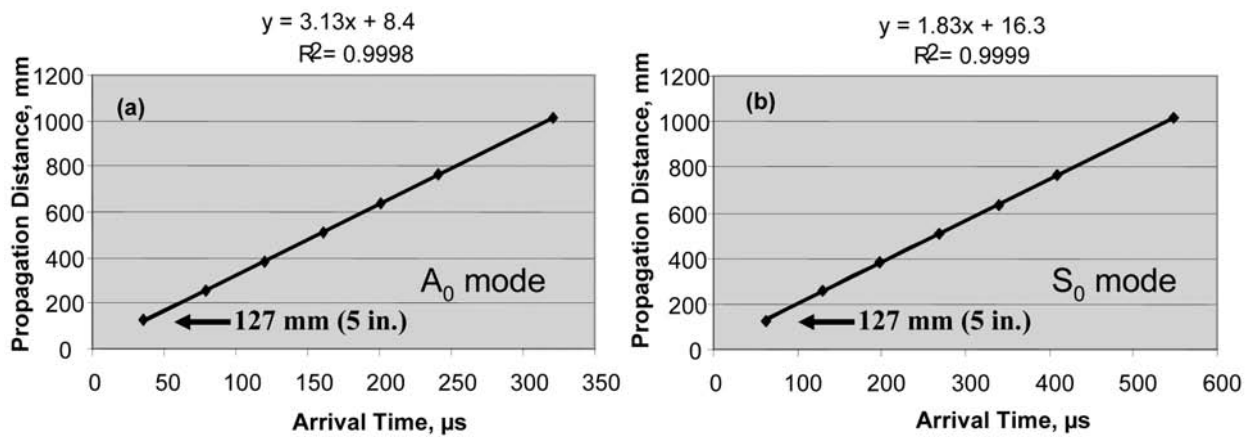


Fig. 15 Plot of propagation distance versus arrival time determined by WT maximum at 102 kHz; no filter data for an out-of-plane source depth of (a) 24.15 mm and A<sub>0</sub> mode and (b) 7.72 mm and S<sub>0</sub> mode; and equation of “fit” with correlation coefficient.

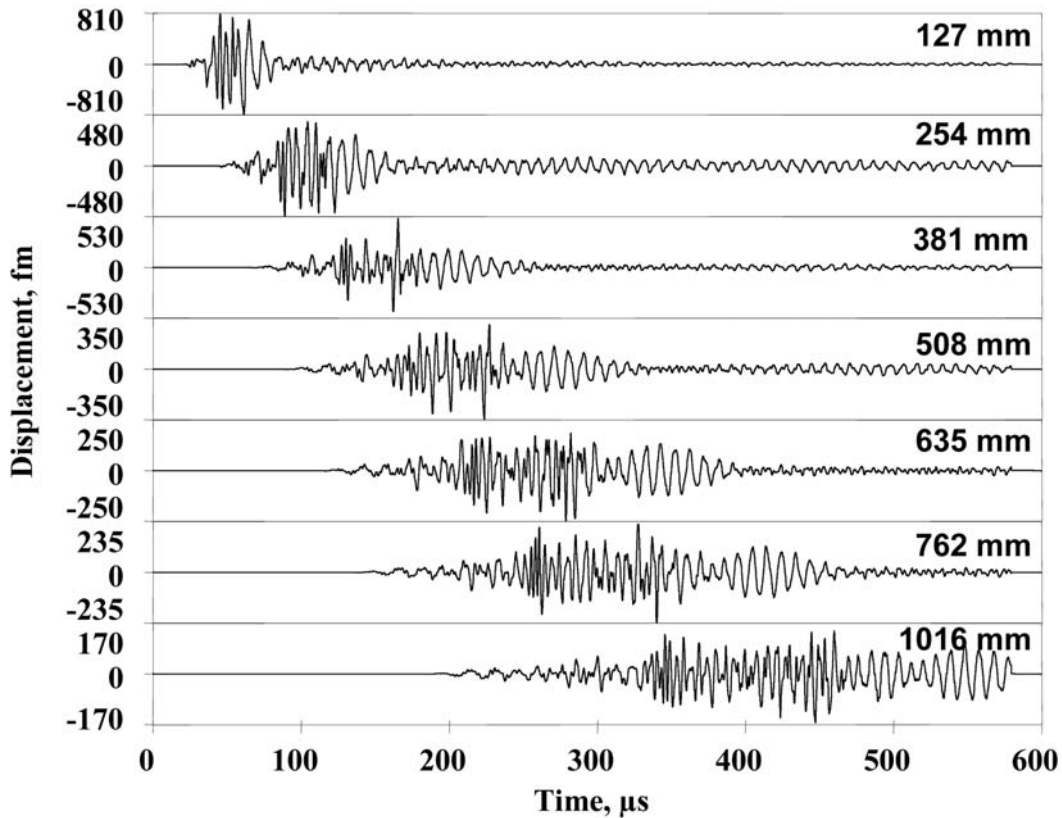


Fig. 16 Dispersion of AE signals at propagation distances shown for source depth of 7.72 mm; 40-kHz high-pass data.

propagation distance increased from 127 mm to 1016 mm. Further, over this range of distances the signal peak amplitudes decreased by 12 dB to 19 dB from the first distance to the last for the different depths and filter ranges. These large changes in durations and signal peak amplitudes did not affect the determination of accurate mode arrival times.

Two additional frequencies were examined (190 kHz and 50 kHz). In both cases, the mode that led to the WT peak magnitude was not constant at all the propagation distances for some source depths. Thus these frequencies were not pursued in detail.

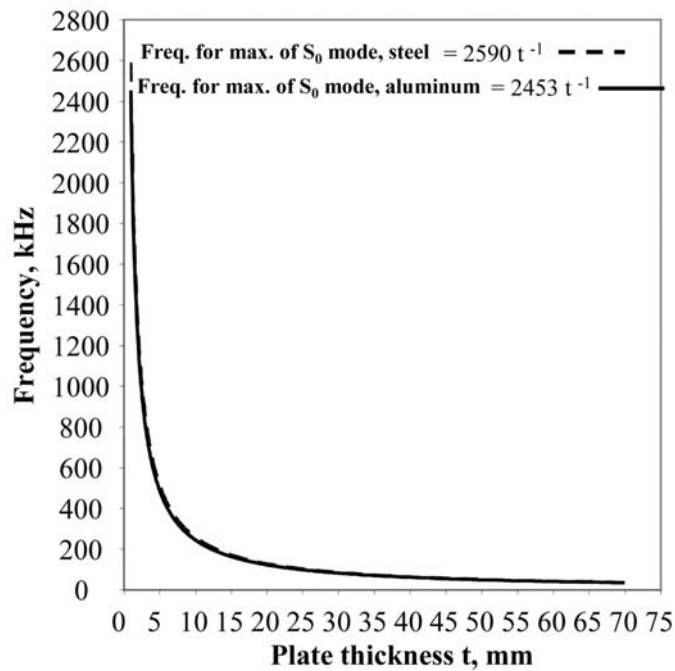


Fig. 17 Frequency of maximum WT intensity of the  $S_0$  mode as a function of plate thickness for aluminum and steel plates.

Since the region of the  $S_0$  group velocity curve that gave rise to the WT peak at 102 kHz is the same region that provided accurate arrival times for this mode at 522 kHz in the 4.7-mm thick aluminum plate [1], Fig. 17 was created to show how this frequency changes with plate thickness for both steel and aluminum. Potentially this figure could be used to select appropriate frequencies for plates of steel or aluminum of other thicknesses. These frequencies could be used to determine accurate arrival times for the  $S_0$  mode (and at depths near a plate surface the  $A_0$  mode, as demonstrated in this paper) by a WT or other equivalent approaches.

### Application to Source Location and Related Mode Identification of the Single Frequency (102 kHz) Determined Arrival Times

Because in an actual experimental AE application the source depth for each AE event is unknown, a WT peak-determined arrival time at 102 kHz could be associated with either the  $A_0$  or the  $S_0$  mode (Note as pointed out before, no WT peaks at 102 kHz were observed with the other possible mode,  $A_1$ ). Thus, we examined a possible approach that would allow determination of the mode that resulted in the WT-determined peak arrival time for a particular experimental AE event. It was assumed that the signals from the event were recorded at four different sensors in a location array. Using the available different propagation distances, a series of cases was examined with different placements of the sensors around a fixed source location. Figure 18 shows a particular case of the arrangement of the sensors around a source location (indicated by **X** in the figure). The arrival time information in Table 3 (40-kHz high-pass data) was used to calculate relative arrival times for the appropriate propagation distances. For each sensor array case, the arrival times selected corresponded to those for two different source depths that provided data for the two possible modes ( $A_0$  and  $S_0$ ). Planar source location software [15] was used to calculate the location by using each of the two possible group velocities (those found from the slope plots referred to earlier). Thus, for each case, a total of four locations were calculated with the 102 kHz data. These calculations were: (i)  $A_0$  mode arrival times and  $A_0$  mode velocity, (ii)  $A_0$  mode arrival times and  $S_0$  mode velocity, (iii)  $S_0$  mode arrival times and  $A_0$  mode velocity, and (iv)  $S_0$

mode arrival times and  $S_0$  mode velocity. From the results for each location calculation, the radius error from the actual known location to the calculated one was determined. It was found that the mode velocity that gave the least radius error corresponded to the known actual mode that corresponded to the set of WT peak determined arrival times for that mode.

Table 5 Sensor coordinates, arrival times, radius errors and uncertainty (“Lucy”)\*.

Case no.	Array of sensor coordinates x/y (mm)				Relative arrival times at each sensor for the modes, $A_0/S_0$ ( $\mu$ s)				Radius error at specified mode velocity (mm)		“Lucy” values at specified mode velocity (mm)	
	#1	#2	#3	#4	#1	#2	#3	#4	$A_0$	$S_0$	$A_0$	$S_0$
1	1410	1011.1	1697	906.8	0	44.5	122.3	164.7	<b>9.62</b> <sup>§</sup>	115 <sup>#</sup>	<b>2.2</b>	17.6
	1356.4	1204.8	1942.3	2219	0	67.7	208.4	279	241 <sup>§§</sup>	<b>2</b> <sup>##</sup>	15	<b>1.6</b>
2	1117.6	1327.7	1443.7	737.4	0	36.6	158.9	201.3	<b>8.65</b>	145	<b>0.30</b>	55.3
	1447.7	1294.4	2118	2114.5	0	66.5	274.9	345.5	—	<b>4.2</b>	—	<b>1.01</b>
3	1121.9	1326.1	1595	886.6	0	36.6	81.1	120.6	<b>4.6</b>	105	<b>5.4</b>	33.6
	1442.4	1293.6	1586.9	1908	0	66.5	134.2	204.5	166	<b>5.6</b>	103	<b>1.5</b>
4	1190.6	1385.2	719.4	2234.1	0	36.6	120.6	279.4	<b>5.2</b>	190	<b>1.7</b>	152
	1647.7	1331.7	1433.2	1570.1	0	66.5	204.5	484.6	—	<b>4.9</b>	—	<b>0.83</b>
5	1436.6	1092.9	1840.3	586.7	0	39.5	77.8	198.3	<b>5.8</b>	143	<b>2.2</b>	20.4
	1211.1	1032	1656	2319.1	0	70.3	140.7	350.4	234	<b>3.1</b>	8.9	<b>0.78</b>
6	1175.6	1144.1	1585.4	1585.9	0	36.6	81.1	120.6	<b>7.1</b>	90	<b>2.7</b>	41.7
	1643.3	1281.4	1419	1875.6	0	66.5	134.2	204.5	—	<b>5.6</b>	—	<b>0.93</b>
7	1306.3	609.1	1759	823.8	0	158.9	201.3	279.4	<b>4.7</b>	178	<b>0.7</b>	181
	1616.4	1347.9	986.1	2459.9	0	274.9	345.5	484.6	—	<b>3.2</b>	—	<b>0.73</b>
8	1117.1	1467.1	913.3	1622.7	0	44.5	122.3	242.8	<b>8</b>	232	<b>0.3</b>	145
	1756.6	1234.8	967.5	2456.4	0	67.7	208.4	418.1	—	<b>0.9</b>	—	<b>1.9</b>
9	1444.1	1070.7	623.6	1983.7	0	84	122.3	242.8	<b>5.2</b>	210	<b>4.7</b>	95.4
	1405.9	1038.2	1744.3	2193.2	0	138	208.4	418.1	68.3	<b>2</b>	326	<b>0.2</b>
10	1085	937.4	1702.6	1839.9	0	44.5	84	122.3	<b>9.1</b>	73	<b>0.55</b>	31.1
	1739.6	1267.6	1367.9	1658.2	0	67.7	138	208.4	142	<b>2.2</b>	49.4	<b>0.22</b>

\* Actual source coordinates for all cases  $x = 1219.2$  mm and  $y = 1524.0$  mm

— ... No result

§ With velocity 3160 m/s for  $A_0$  mode and arrival times for  $A_0$  mode

§§ With velocity 3160 m/s for  $A_0$  mode and arrival times for  $S_0$  mode

## With velocity 1828 m/s for  $S_0$  mode and arrival times for  $S_0$  mode

# With velocity 1828 m/s for  $S_0$  mode and arrival times for  $A_0$  mode

Table 5 provides a summary from a series of ten cases. The table shows the coordinates of the four sensors in each array along with the relative arrival times for each mode. The table also shows the radius errors for each of the two possible group velocities. Due to the nature of the database used for these calculations, the source location ( $x = 1219.2$  mm,  $y = 1524$  mm) was always the same for each case.

The results summarized in Table 5 indicate that accurate source locations (smaller radius of location errors, bold values) were consistent with the correct choice of the mode and associated group velocity. In some cases in this table, when the incorrect group velocity was used, the

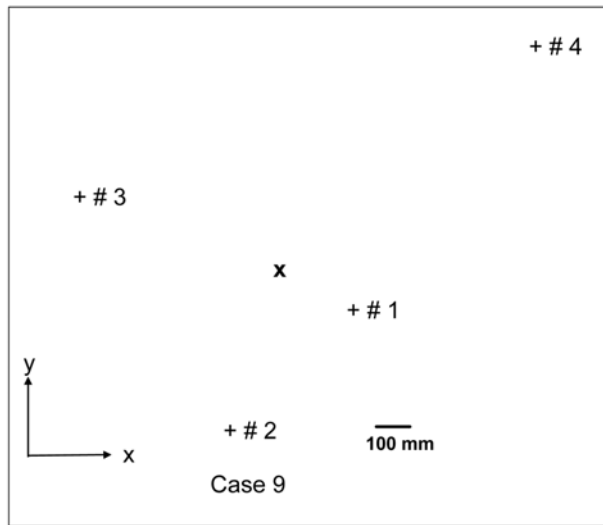


Fig. 18 Arrangement of sensors (#1, #2, #3, #4) around source location  $X$  ( $x = 1219.2$  mm,  $y = 1524$  mm). Scale shown as well as the directions of the  $x$  and  $y$  axis (origin not shown).

source-location software did not generate a result. Examination of the input data for those cases showed that the equation of the hyperbola that should locate the locus of possible locations of the source between each two-sensor set had a negative sign for the distance from the closest sensor to the hyperbola. This situation typically occurred when the higher  $A_0$ -mode velocity was used with the slower velocity  $S_0$ -mode arrival times. In addition, significant errors in the calculated source locations were the result of the use of the wrong mode and its associated group velocity. These facts indicated that a measurement of the “uncertainty” level of the iterative source location calculation might be used to determine the correct mode and associated velocity for a particular set of arrival times from an experimental source at an unknown depth. The source-location software [15] automatically provided an “uncertainty” value for each location calculation. Table 5 also shows this “uncertainty” parameter (called “Lucy” [for location uncertainty] by the software developer) for the two possible group velocities in each case. According to the software designer [15] “Lucy describes how well a calculated source position fits with the measured arrival time differences.” The value for “Lucy” is calculated from

$$\text{Lucy} = \left\{ \frac{1}{[n-1]} * \left[ \sum (D_i - P_i)^2 \right] \right\}^{1/2}. \quad (2)$$

In this equation, the sum is from  $i = 2$  to  $n$ , where  $n$  is the number of sensors hit by the signals from each source event. The values of  $D_i$  are calculated from

$$D_i = dt_i * v, \quad (3)$$

where  $dt_i$  is the signal arrival time difference relative to the first hit sensor ( $n = 1$ ), and  $v$  is the group velocity. The values of  $P_i$  are calculated from

$$P_i = R_i - R_1, \quad (4)$$

where  $R_i$  is the distance from the calculated source location to each of the sensors. “Lucy” can be determined as part of the result of a location calculation only if an event consists of at least one more hit than the minimum required to determine a location (in the cases considered here, three hits are the minimum for planar location). Clearly the table shows the “Lucy” value is the smallest (bold values) for the velocity that resulted in the least radius error. Thus, either the smallest “Lucy” value (directly identifies the correct mode) or no result (identifies the alternate mode velocity is correct) for the location calculation identified the correct mode and associated group velocity for the wide variety of sensor arrays examined.

Results equivalent to those in Table 5 were obtained for the other two frequency ranges (no filter and 100 kHz to 300 kHz). These results (not included in this paper) were similar to those shown in Table 5, and the conclusions relative to the relation between the smallest “Lucy” values, smallest radius error and correct group velocity were similar. In addition for all three frequency ranges, the average radius errors for the slower velocity mode were only about one half the average radius errors for the faster velocity mode. For example, the average radius errors respectively for the slow versus fast velocities were respectively 3.6 mm (standard deviation of  $\pm 1.7$  mm) and 7.1 mm (standard deviation of  $\pm 1.7$  mm) for the 100-kHz to 300-kHz bandpass data.

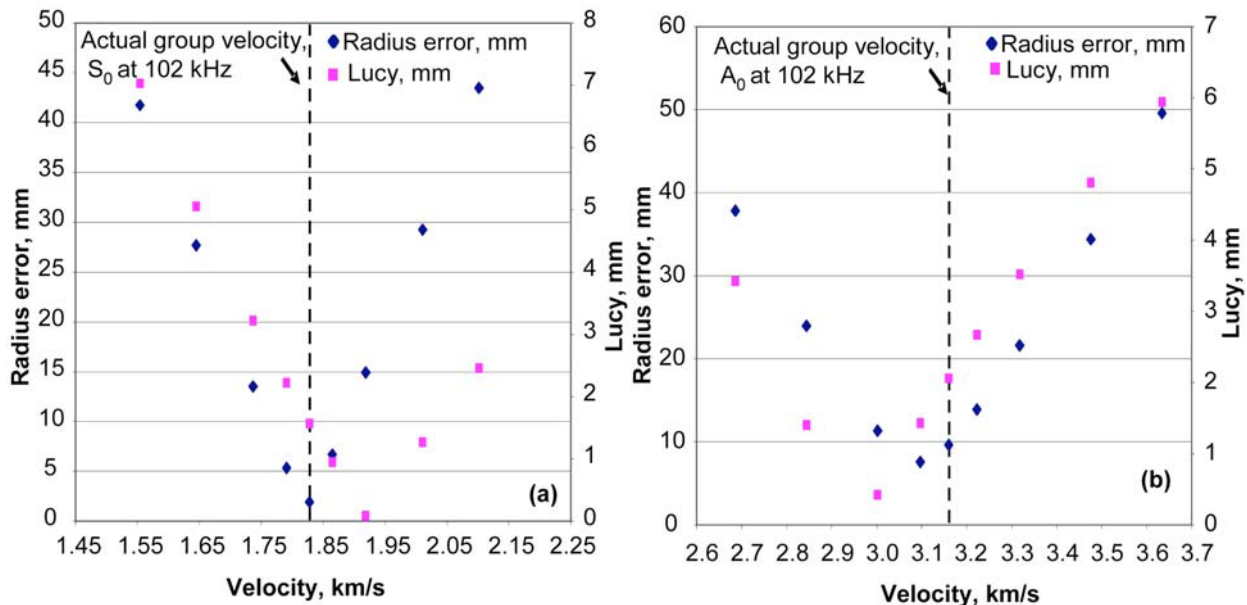


Fig. 19 Radius error and “Lucy” value versus group velocity in the vicinity of the correct velocity. Results for case 1 in table 5 with (a) for the  $S_0$  mode and (b) for the  $A_0$  mode.

The sensitivity to small errors in the velocity used in the approach (described above) to determine the correct mode and group velocity (for a set of arrival time differences) was studied. Calculations of the radius errors and “Lucy” values were made when the velocity was in error relative to the correct value for the mode. The velocity errors examined were  $\pm 2\%$ ,  $5\%$ ,  $10\%$ , and  $15\%$  from the correct mode velocities. Figure 19 shows a typical result of how the radius error and the “Lucy” values varied as a function of the group velocity used in the location calculation. Figure 19(a) shows the results for the slow velocity mode ( $S_0$ ), and Fig. 19(b) shows the results for the fast velocity mode ( $A_0$ ). These results for case 1 in Table 5 (using the 40 kHz high-pass data) show that the radius error and the “Lucy” values have minima near the correct velocity. It is worth noting that the minima of both parameters are not at exactly the same velocity. The fact that the radius error and “Lucy” values have minimum values near the correct velocity indicates that in experimental situations where there may be small errors in the mode velocities used, the technique proposed here could be expected to continue to result in correct identification of the mode that resulted in the set of arrival times for a particular AE event.

The method described in this section of the paper could be automated in software. Arrival times at an appropriate frequency could be determined by advanced signal processing of the digitized signals from each sensor in a location array for each event. Then location calculations could be made by using the two possible group velocities at the appropriate frequency. The

location calculation result that yielded the lowest “uncertainty” or the calculation that produced a location (no location result for one velocity) could then be selected. Thus the use of nonresonant sensors could improve the accuracy of source location even in thick plates, as has been shown in thin plates [16].

## Conclusions

- The wavelet transforms of signals from in-plane and out-of-plane dipoles at the same depth demonstrates mostly similar regions of signal intensity.
- For sources near the top or bottom surface of the thick plate, the most intense portion of the  $A_0$  mode is at frequencies below those normally used in AE monitoring.
- For sources near a surface, the signal from a sensor on that surface exhibits a Rayleigh wave at frequencies above about 340 kHz
- The signals from the 25.4-mm thick plate have multiple intense regions (combinations of mode and frequency) as the depth of the source varies.
- The choice of a frequency of 102 kHz provides wavelet transform peak determined arrival times for mostly the  $S_0$  mode as the depth of the source varies. For sources near a plate surface, the wavelet transform peak at this frequency corresponds to the  $A_0$  mode. No maximum peaks were observed for the  $A_1$  mode at this frequency.
- Over a wide range of propagation distances (127 mm to 1016 mm) and source depths, the wavelet transform peak at 102-kHz frequency provided accurate arrival times, since the slope of plots of the propagation distance versus these arrival times provided group velocities very close to the theoretical values.
- For sources at an unknown depth recorded with at least a four-sensor array, the calculation of the planar location of the source from the WT peak arrival times at 102 kHz using the two possible group velocities yields two different locations or in some cases only a location with one of the two group velocities. The lowest value of the “uncertainty” or the only velocity that produced a location result from the two source location calculations corresponds to the correct location and the correct mode (and associated group velocity) of the arrival times.
- This method for the determination of the correct mode of the arrival times and associated group velocity could be automated to process digitized signals to significantly improve accuracy of source location even in thick plates when non-resonant AE sensors are used.
- This method is not dependent on the use of exactly the correct group velocity for the two modes at 102 kHz.

## Acknowledgements

The development of the finite element code and case runs by Dr. John Gary (NIST retired) are acknowledged. Filtering of the FEM results by Ms. Abbie O’Gallagher, NIST Boulder, CO is appreciated. Also the analysis efforts of Mr. Matthew Papa (University of Denver, Mechanical Engineering undergraduate) are appreciated. Finally, the private communications listed in the references are highly appreciated.

### *Copyright Notice*

This paper is a contribution of the U.S. National Institute of Standards and Technology; not subject to copyright in the United States. Trade and company names are included only for complete scientific/technical description; endorsement is neither intended nor implied.

## References

1. Hamstad, M.A., K.S. Downs and A. O’Gallagher, “Practical aspects of acoustic emission source location by a wavelet transform,” *J. of Acoustic Emission*, **21** (2003), 70-94 and A1-A7.
2. Downs, K.S., M.A. Hamstad and A. O’Gallagher, “Wavelet transform signal processing to distinguish different acoustic emission sources,” *J. of Acoustic Emission*, **21** (2003), 52-69.
3. Hamstad, M.A. and A. O’Gallagher, “Effects of noise on Lamb-mode acoustic-emission arrival times determined by wavelet transform,” *J. of Acoustic Emission*, **23** (2005), 1- 24.
4. Hamstad, M.A. and A. O’Gallagher, “Modal-based identification of acoustic emission sources in the presence of electronic noise,” *J. of Acoustic Emission*, **22** (2004), 1-21, A1-A7.
5. Bayray, Mulu and Franz Rauscheer, "Wavelet transformation analysis for experimental AE waveforms on steel pressure vessel," *J. of Acoustic Emission*, **22** (2006), 22-43.
6. Hamstad, M. A., J. Gary and A. O’Gallagher, "Far-field acoustic emission waves by three-dimensional finite element modeling of pencil breaks on a thick plate," *J. of Acoustic Emission*, **14**(2) (1996), 103-114.
7. Hamstad, M.A., A. O’Gallagher and J. Gary, "Modeling of buried acoustic emission monopole and dipole sources with a finite element technique," *J. of Acoustic Emission*, **17**(3-4), (1999), 97-110.
8. Burridge, R. and L. Knopoff, “Body force equivalents for seismic dislocations,” *Bulletin Seismic Society of America*, **54** (1964), 1875-1914.
9. Kolsky, H., “*Stress Waves in Solids*,” Dover Publications, New York (1963).
10. Vallen, J., AGU-Vallen Wavelet transform software, version R2007.0309, Vallen-Systeme GmbH, Icking, Germany (2007). Available at <http://www.vallen.de/wavelet/index.html>
11. Cho, Hideo, Private communication, Aoyama Gakuin University, Sagamihara, Japan (2006).
12. Vallen, Jochen and Gabriel Corneanu, Private communication, Vallen-Systeme GmbH, Icking, Germany (2006).
13. Hamstad, M.A., A. O’Gallagher and J. Gary, "Examination of the Application of a Wavelet Transform to Acoustic Emission Signals: Part 1. Source Identification," *J. of Acoustic Emission*, **20** (2002), 39-61.
14. Sachse, Wolfgang and Yih-Hsing Pao, “Signals in the far-field of an AE source,” *Ultrasonics International 1981: Conference Proceedings*, IPC Science and Technology Press, Guildford, Surrey, UK, 1981, pp. 116-122.
15. Vallen, Jochen, Private communication, Vallen-Systeme GmbH, Icking, Germany (2001).
16. Ziola, Steven M., "Source location in thin plates using crosscorrelation," Ph.D. Thesis, Naval Postgraduate School, Monterey, CA., (1991).